

# Electrocaloric effect and energy-storage performance in grain-size-engineered PBLZT antiferroelectric thick films

Hongcheng Gao<sup>1</sup> · Xihong Hao<sup>1</sup> · Qiwei Zhang<sup>1</sup> · Shengli An<sup>1</sup> · Ling Bing Kong<sup>2</sup>

Received: 18 April 2016 / Accepted: 31 May 2016 / Published online: 4 June 2016  
© Springer Science+Business Media New York 2016

**Abstract** The effects of grain size on dielectric properties, energy-storage performance and electrocaloric effect (ECE) of  $\text{Pb}_{0.85}\text{Ba}_{0.05}\text{La}_{0.10}(\text{Zr}_{0.90}\text{Ti}_{0.10})\text{O}_3$  (PBLZT) antiferroelectric thick films were systematically studied. As the grain size was increased, dielectric constant of the thick films was increased, while their critical breakdown field was decreased. A giant reversible adiabatic temperature change of  $\Delta T = 19.9^\circ\text{C}$  at room temperature was achieved in the PBLZT AFE thick film with a grain size of  $0.59\ \mu\text{m}$ . However, a huge recoverable energy-storage density of  $33.6\ \text{J}/\text{cm}^3$  and a high efficiency of 73 % were observed in the film with the smallest grain size of  $0.19\ \mu\text{m}$  at its breakdown field, because of its excellent electric field endurance. In addition, all the samples had a low leakage current density of below  $10^{-6}\ \text{A}/\text{cm}^2$  at room temperature. These results indicated that our PBLZT AFE thick films could be a promising candidate for applications in high energy-storage density capacitors and solid-cooling devices by properly controlling their grain size.

## 1 Introduction

Antiferroelectricity (AFE) was first formally defined in 1951 by Kittel [1], in which the neighboring dipoles were alternately aligned in opposition directions, so that no net macroscopic remanent polarization ( $P_r$ ) exists in the AFE phase. In the same year, the first AFE,  $\text{PbZrO}_3$ , was reported by Sawaguchi [2, 3]. Since then,  $\text{PbZrO}_3$ -based AFE materials were attracted much attention because of their unique phase transition process, especially the transition between AFE and ferroelectric (FE) phase under the application of electric field, temperature and stress or their combination. It was reported that, during the phase switching process, considerable charge and discharge current, huge pyroelectric coefficient, noticeable strain and giant electrocaloric effect (ECE) in the AFEs could be realized [4–8]. Therefore, the AFE has a strong potential for application in multifunctional devices, such as high energy-storage capacitors and solid-state cooling components [9–11].

In the past decades, significant efforts have been made to improve the energy-storage performance and ECE of AFE materials. However, the attention has been mainly focused on bulk ceramics and thin films, but they still cannot be used for the practical applications [12–15]. Bulk ceramics usually exhibit very low energy-storage density and weak ECE due to their relatively low breakdown strengths (BDS). Moreover, bulk ceramics require relatively high operating voltages because of their bulky format [16, 17]. Although thin films have shown large energy-storage density and superior ECE [18, 19], the overall energy stored and heat-sinking capacity were limited by their small overall volumes. As a result, AFE thick-films would be a promising candidate to address the problems of bulk ceramics and thin films, for applications in high energy-storage capacitors and solid-state cooling devices.

✉ Xihong Hao  
xhhao@imust.cn

<sup>1</sup> School of Materials and Metallurgy, Inner Mongolia University of Science and Technology, Baotou 014010, China

<sup>2</sup> School of Materials Science and Engineering, Nanyang Technological University, 50 Nanyang Avenue, Singapore 639798, Singapore

Various factors have been evaluated in influencing the energy-storage performances and ECEs of AFE thick films, such as chemical composition, type of electrode material, breakdown strength and orientation [20–23]. In fact, grain size is also an important factor to influence the energy-storage performance and ECE, through its effect on the dielectric properties of materials [24–26]. For example, ECE of  $0.9\text{Pb}(\text{Mg}_{1/3}\text{Nb}_{2/3})\text{O}_3-0.1\text{PbTiO}_3$  ceramics could be greatly improved by regulating the grain size [27]. However, to the best of our knowledge, the effect of grain size on energy-storage performance and ECE of AFE thick films has not been reported. Thus, in this work,  $\text{Pb}_{0.85}\text{Ba}_{0.05}\text{La}_{0.10}(\text{Zr}_{0.90}\text{Ti}_{0.10})\text{O}_3$  AFE thick films with different grain sizes were prepared by using a sol–gel route. The effect of grain size on electrical properties, energy-storage performance and ECE of the thick films were systematically investigated, with an aim to obtain superior energy-storage density and a huge ECE through the proper control of grain size.

## 2 Experimental procedure

$\text{Pb}_{0.85}\text{Ba}_{0.05}\text{La}_{0.10}(\text{Zr}_{0.90}\text{Ti}_{0.10})\text{O}_3$  (PBLZT) thick films were grown on  $\text{LaNiO}_3(100)/\text{Si}(100)$  substrates by using a sol–gel method. Lead acetate trihydrate [ $\text{Pb}(\text{CH}_3\text{COO})_2 \cdot 3\text{H}_2\text{O}$ ], lanthanum acetate hydrate [ $\text{La}(\text{CH}_3\text{COO})_3 \cdot x\text{H}_2\text{O}$ ], zirconium propoxide [ $\text{Zr}(\text{OC}_3\text{H}_7)_4$ ], titanium isopropoxide [ $\text{Ti}[\text{OCH}(\text{CH}_3)_2]_4$ ] and barium acetate [ $\text{Ba}(\text{CH}_3\text{COO})_2$ ] were used as the raw materials. Acetate and deionized water were used as solvents. Firstly, lead acetate trihydrate, barium acetate and lanthanum acetate hydrate were dissolved in acetic acid in a ratio according to the predetermined composition. To compensate for the lead loss during sintering and prevent the formation of pyrochlore phase, 20 mol% excess of lead was used. The solution was distilled at 110 °C to remove water. After the solution was cooled to room temperature, zirconium propoxide and titanium isopropoxide were added, stirring for 30 min. During the mixing process, a certain amount of distilled water was added to stabilize the solution. In order to improve mechanical properties of the gel film, lactic acid and ethylene glycol were added into the solution and the molar ratio to lead was 1:1. Finally, the concentration of the PBLZT sol was adjusted to 0.5 M by adding a proper amount of acetic acid. Conductive  $\text{LaNiO}_3$  (LNO) with (100) orientation were used as bottom electrodes, which were deposited on Si (100) substrates by using the chemical solution deposition route similar to that reported in Ref. [8].

After being aged for 24 h, the solution was used to deposit PBLZT thick films on the  $\text{LaNiO}_3/\text{Si}$  (100) substrates by using a multiple layer spin-coating procedure. Each wet layer was formed by spin-coating at 3000 rpm for

40 s. In order to form a uniform film, every wet film was dried at 350 °C for 10 min and subsequently pyrolyzed at 600 °C for 10 min to remove organics. The spin coating and heat-treatment were repeated several times to obtain samples with desired thicknesses. In order to prevent the loss of lead during the final annealing, a capping layer of PbO was coated on the PBLZT films, with 0.4 M lead acetate trihydrate solution. In order to obtain thick films with different grain sizes, the samples were annealed at 700 °C for 10, 20 and 30 min. Final thickness of the thick films was about 1.5  $\mu\text{m}$  estimated from their cross-sectional SEM images.

Crystallographic properties and surface morphology of the PBLZT thick films were examined by using X-ray diffractometer (XRD Bruker D8 Advanced Diffractometer, German) and field-emission scanning electron microscopy (FE–SEM ZEISS Supra 55, German), respectively. To measure electrical properties, gold pads of 0.20 mm in diameter were coated on the film surface as top electrodes by using a DC sputtering through a metal shade mask with circular holes. Temperature, frequency and electric field dependences of dielectric properties of the thick films were measured by using a computer-controlled Agilent E4980A LCR analyzer. Field-induced hysteresis loops and leakage current characteristics of the PBLZT thick films were measured by using a Ferroelectric tester (Radiant Technologies, Inc., Albuquerque, USA). The energy-storage performance and ECE of the films were calculated according to the  $P$ – $E$  results.

## 3 Results and discussion

Surface FE–SEM images of the thick films with different annealing times are shown in Fig. 1a–c. Obviously, all the samples have a smooth, dense and void-free surface morphology. Moreover, with the annealing time increasing, the grain size increases gradually, as shown in Fig. 1d–f. The average grain size at the surface of the films is 0.19, 0.40 and 0.59  $\mu\text{m}$  for the films annealed for 10, 20 and 30 min, respectively, which was calculated by using the Nano Measurer software. It should be noted here that, although the grain size at the top and bottom of the films may be slightly different, the films with a longer final annealing time must possess a larger grain size. The variation of the grain size in the films is caused by the repeated spin-coating and heat-treatment procedure. The cross-sectional SEM images of the thick films are presented in Fig. 1g–i, indicating that all the films possess a uniform and dense microstructure with a thickness of about 1.5  $\mu\text{m}$ . Moreover, the columnar-like growth is found in the PBLZT AFE thick films, indicating that the nucleation and growth of the crystals may initiate from the bottom electrodes [28].

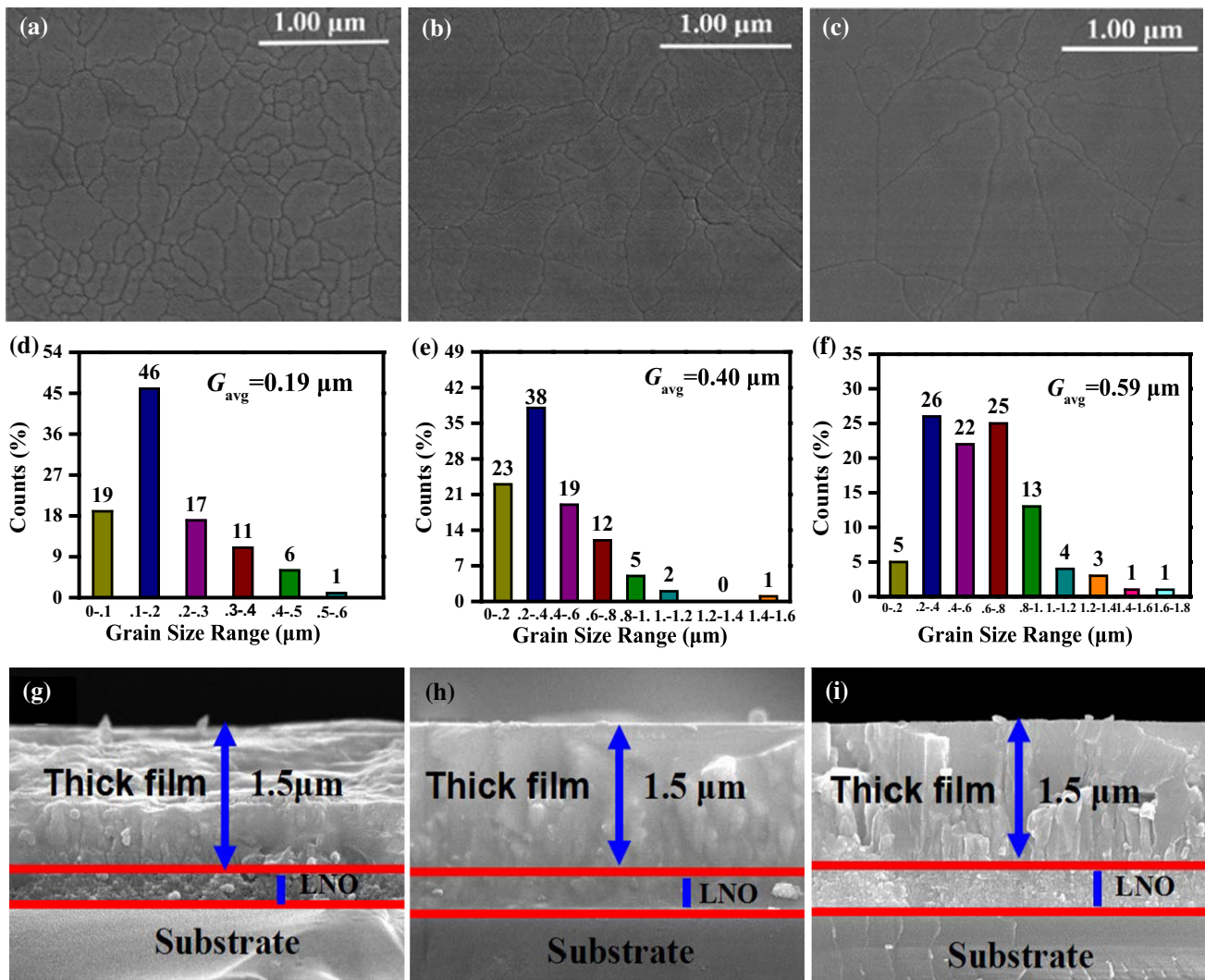


**Fig. 1** a–c surface FE–SEM images of the PBLZT AFE thick films with different grain sizes. d–f Average grain sizes of the films. g–i Cross-sectional SEM images of the films

Figure 2a shows XRD patterns of the PBLZT AFE thick films. Evidently, all the samples display well-developed crystallinity with a pure perovskite phase. Moreover, all the films show a high (100)-orientation, due to the small lattice mismatch with the (100)-orientated LNO bottom electrodes [29–31]. In order to estimate the degree of the (100) orientation, the preferential ratios ( $\alpha$ ) are defined by the diffraction intensity ratio of the (100) peak to the (100), (110), and (111) peaks [32, 33]:

$$\alpha = \frac{I(100)}{\{I(100) + I(110) + I(111)\}} \quad (1)$$

It is found that the (100)-preferential ratio increases from 0.75 to 0.89, as the grain size is increased from 0.19 to 0.59 μm, as shown in Fig. 2b. This result indicates that the longer annealing time is helpful to the growth of (100) orientation.

Frequency-dependent dielectric constant and dielectric loss of the PBLZT AFE thick films, measured over 1–1000 kHz at room temperature, are plotted in Fig. 3. It is seen that the dielectric constant gradually decrease for all the samples with increasing frequency. The declined tendency is caused by the long-time polarization process of some frameworks, such as space charges, which have no contribution to the overall polarization at higher frequency [8]. It is well known that the values of the dielectric constant are strongly related to microstructure and grain size [34]. Generally, larger grain size leads to higher dielectric constant and dielectric loss [35]. This is because small grain corresponds to large number of grain boundaries, while large number of grain boundaries usually leads to low polarization intensity [35–37]. Obviously, the similar trend is also observed in the present work. For example, as shown in the inset of Fig. 3, the dielectric constants at

**Fig. 2** **a** XRD patterns of the PBLZT AFE thick films with different grain sizes. **b** The corresponding (100)-preferential ratios ( $\alpha$ ) of the films

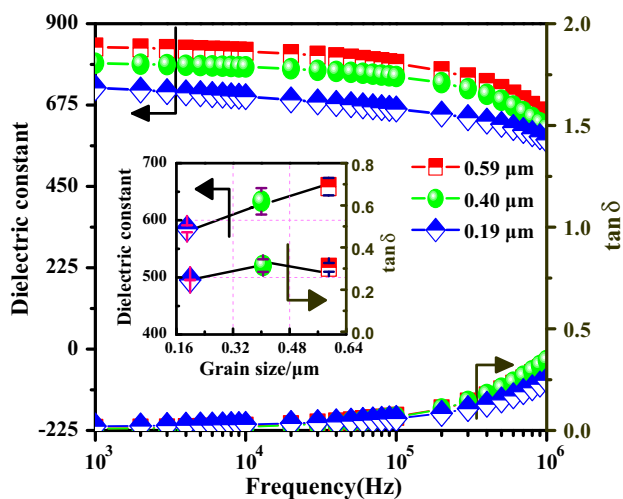
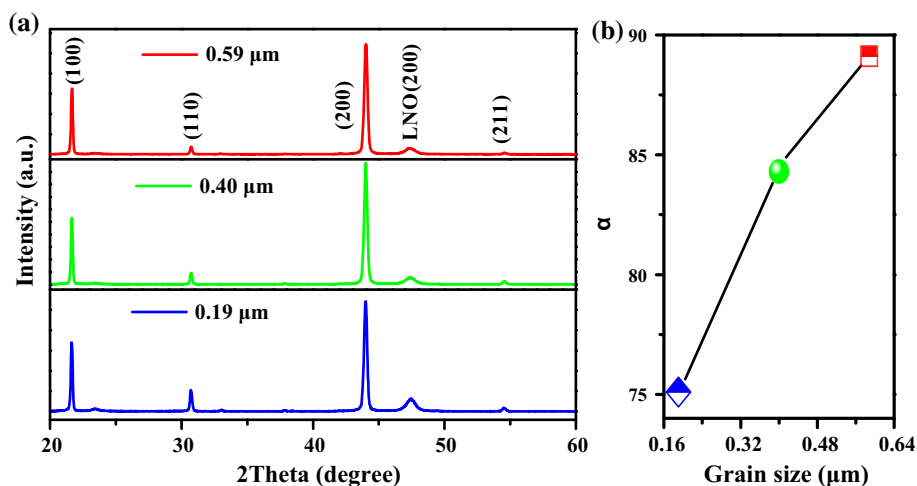


**Fig. 3** Frequency-dependent dielectric constant and dielectric loss of the PBLZT AFE thick films at room temperature, with the inset showing the corresponding dielectric constants and dielectric loss at 1 MHz

1 MHz are 585, 633 and 658, for the thick films with grain sizes of 0.19, 0.40 and 0.59  $\mu\text{m}$ , respectively.

Figure 4a shows  $P$ - $E$  loops of the PBLZT AFE thick films, which were measured at 1 kHz and 900 kV/cm. It is clear that all the samples exhibit a slim double loop, indicating their AFE nature. Both the maximum polarizations ( $P_{\text{max}}$ ) and the remanent polarization ( $P_r$ ) increase with increasing grain size, as shown in Fig. 4b. For example, the average values of  $P_{\text{max}}$  are 53.7, 61.8 and 67.0  $\mu\text{C}/\text{cm}^2$  for the films with grain sizes of 0.19, 0.40 and 0.59  $\mu\text{m}$ , respectively. Evidently, the variation tendency of the polarization are same to the changes of the dielectric constant of the thick films, because of relational expression  $P = (\epsilon_r - 1)\epsilon_0 E$  ( $\epsilon_0$  is dielectric constant of free space,  $\epsilon_r$  is the relative dielectric constant and  $E$  is the applied electric field). Dielectric constant and the dielectric loss as a

function of bias field of the PBLZT thick films, measured at 100 kHz at room temperature, are shown in Fig. 4c. The DC field was stepped at a time lag of 0.5 s according to the following measurement mode:  $E_{\text{max}}$  to zero, zero to  $-E_{\text{max}}$  and  $-E_{\text{max}}$  to  $E_{\text{max}}$ . All the  $\epsilon_r - E$  curves show a double butterfly behavior, which corresponds to the forward and reverses switchings between the AFE and FE phases. The Fig. 4d depicts the forward switching field ( $E_{\text{AFE-FE}}$ ) and the backward switching ( $E_{\text{FE-AFE}}$ ) field, as a function of grain size. It can be seen that both  $E_{\text{AFE-FE}}$  and  $E_{\text{FE-AFE}}$  increase with the grain size increasing. This result implies that a large grain size is likely to stabilize the AFE state.

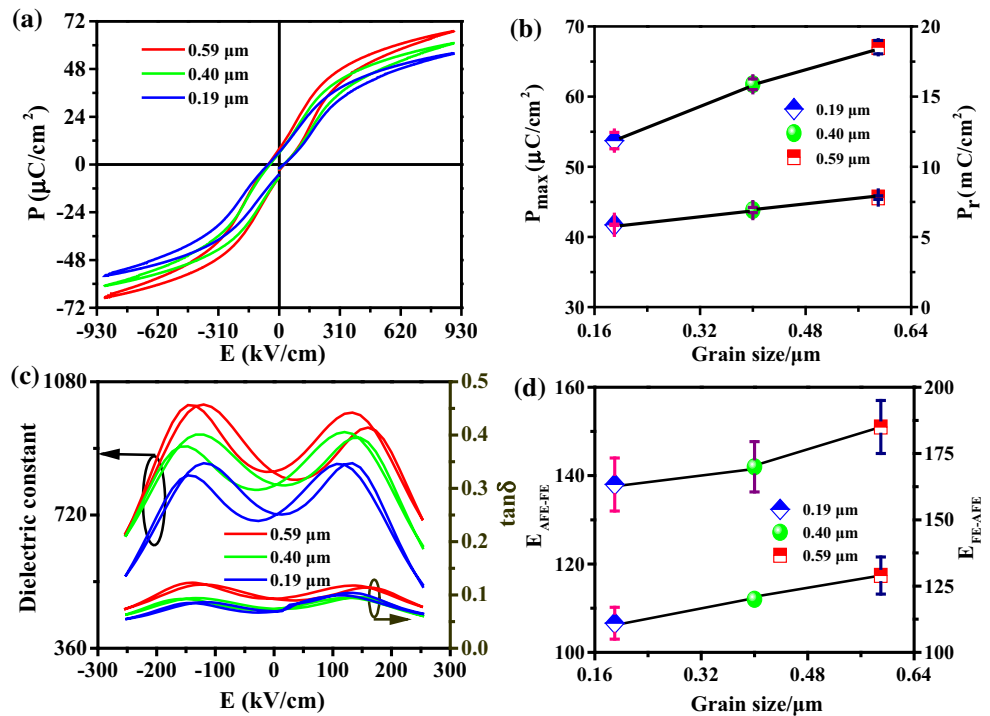
Figure 5a shows temperature-dependent dielectric constant of the PBLZT AFE thick films at 100 kHz from the room temperature to 175  $^{\circ}\text{C}$ . Obviously, the dielectric constant in all the cases first increases gradually, and then decreases, with the temperature increasing. The maximum dielectric constant is arrived at the Curie point, corresponding to the AFE to paraelectric (PE) phase transition, which is 113.8, 121.3 and 118.5  $^{\circ}\text{C}$  for the films with grain sizes of 0.19, 0.40 and 0.59  $\mu\text{m}$ , respectively. Moreover, the broadening in the dielectric constant versus temperature curve indicates the typical diffuse phase transition behavior of the thick films [38]. It is well known that the dielectric constant of a normal ferroelectrics and antiferroelectrics above Curie temperature follows the Curie-Weiss law described by [37, 39]:

$$\frac{1}{\epsilon} = \frac{T - T_0}{C}, \quad (2)$$

where  $T_0$  is the Curie-Weiss temperature and  $C$  is the Curie-Weiss constant. The insets in Fig. 5a shows the corresponding plots of temperature versus inverse dielectric constant at 100 kHz fitted to the Curie-Weiss law. Obviously, all the samples have a deviation from the Curie-Weiss law, confirming their diffused phase



**Fig. 4** **a** Room temperature  $P$ – $E$  loops of the PBLZT AFE thick films with different grain sizes. **b** The corresponding saturated polarizations ( $P_s$ ) and remanent polarization ( $P_r$ ). **c** Dielectric constants of the PBLZT AFE thick films as a function of DC electric field at 100 kHz. **d** The corresponding forward phase switching (AFE-to-FE) fields and the reverse backward phase switching (FE-to-AFE) fields



transition characteristics. The dielectric behavior of diffused phase transition has been well described by the modified Curie–Weiss law, which is given by [40–42]:

$$\frac{1}{\varepsilon} + \frac{1}{\varepsilon_m} = \frac{(T - T_m)^\gamma}{C}, \tag{3}$$

where  $T$  is absolute temperature,  $T_m$  is the temperature at maximum dielectric constant,  $\varepsilon$  is dielectric constant,  $\varepsilon_m$  is the maximum dielectric constant at  $T_m$ ,  $C$  is the Curie–Weiss constant and  $\gamma$  is the indicator of the degree of diffuseness in the range  $1 \sim 2$ . Normal ferroelectric phase transition behavior can be described with  $\gamma = 1$ , while complete diffuse phase transition behavior corresponds to  $\gamma = 2$  [43]. Figure 5b shows plots of  $\ln(1/\varepsilon - 1/\varepsilon_m)$  as a function of  $\ln(T - T_m)$  of the PBLZT AFE thick films at 10 kHz by fitting with Eq. (3), in order to determine the exponent  $\gamma$ . It is found that  $\gamma$  are 1.90, 1.91 and 2.08 for the grain sizes of 0.19, 0.40 and 0.59  $\mu\text{m}$ , respectively, indicating the diffuseness is enhanced with increasing grain size.

According to thermodynamic Maxwell relation,  $(\frac{\partial P}{\partial T})_E = (\frac{\partial S}{\partial E})_T$ , reversible adiabatic temperature change  $\Delta T$  and corresponding isothermal entropy change  $\Delta S$ , as a function of applied field change  $E$ , for a material with density  $\rho$  and heat capacity  $C$ , are given by [19, 31, 44]:

$$\Delta T = -\frac{1}{C\rho} \int_{E_1}^{E_2} T \left( \frac{\partial P}{\partial T} \right)_E dE, \tag{4}$$

$$\Delta S = -\frac{1}{\rho} \int_{E_1}^{E_2} \left( \frac{\partial P}{\partial T} \right)_E dE, \tag{5}$$

where  $T$  is operating temperature,  $P$  is maximum polarization at applied electric field  $E$ . The lower integration limit  $E_1 = 200$  kV/cm was selected. The upper integration limit  $E_2 = 1000$  kV/cm represents the maximum field. The values of  $(\frac{\partial P}{\partial T})_E$  were obtained from fourth-order polynomial fits to the  $P(T)$  data, which are extracted from the hysteresis loops. In the temperature range of interest,  $C$  is about 330 J/K/kg for Zr-rich lead-based films, while the peak associated with the transition is  $<10\%$  of the background [44]. The density  $\rho = 8.3$  g/cm<sup>3</sup> is selected for the thick films as reported before [44]. The values of adiabatic temperature change  $\Delta T$  versus temperature for the PBLZT AFE thick films at  $\Delta E = 800$  kV/cm, deduced from Eq. (4), are shown in Fig. 6a. Large  $\Delta T$  values are achieved in a wide range of temperature near room temperature, which is closely related to the FE–AFE phase transition of the thick films. Detailed description on ECE caused by FE–AFE phase transition can be found in our previous work [20]. As expected, the ECE response is enhanced as the grain size increasing. The maximum  $\Delta T$  values at room temperature are 8.9, 17.6 and 19.9  $^\circ\text{C}$  for the grain sizes of 0.19, 0.40 and 0.59  $\mu\text{m}$ , respectively. As the operating temperature is increased, the  $\Delta T$  value gradually decreases, indicating a reduction in entropy change between the AFE and FE phase transition. With

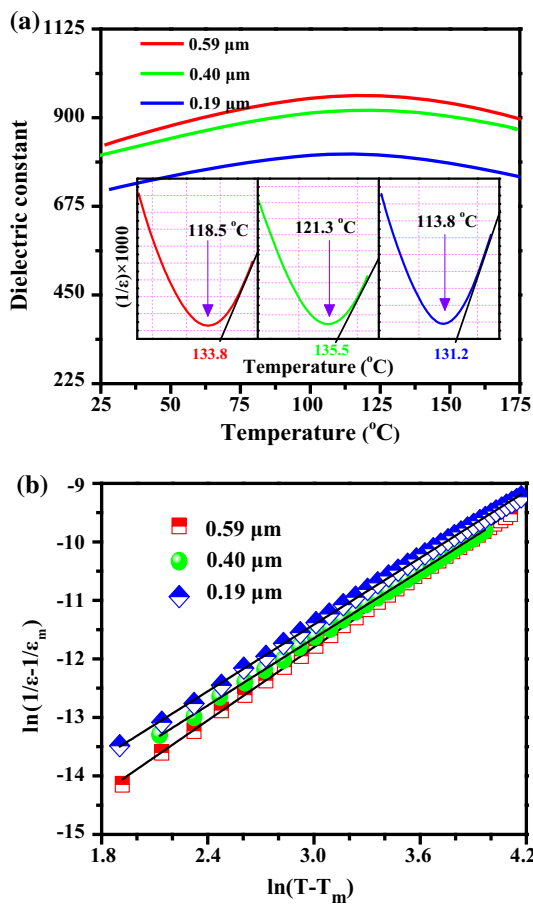


**Fig. 5** **a** Temperature dependences of dielectric constant of the PBLZT AFE thick films at 100 kHz, with the inset showing the inverse dielectric constant ( $1/\epsilon \times 1000$ ) as a function of temperature at 100 kHz for all the samples. **b** Plots of  $\ln(1/\epsilon - 1/\epsilon_m)$  as a function of  $\ln(T - T_m)$  for all the samples at 10 kHz

further increase in temperature, a peak of  $\Delta T$  in the curves is observed in the vicinity of 115 °C, which is believed to be caused by the AFE–PE phase transition. The temperature corresponding to the peak of  $\Delta T$  is slightly lower the Curie temperature, which was consistent with the observation of Tatsuzaki [45]. In fact, the ECE peak can occur either above or below  $T_c$ , but microscopic models of ECE have not been established [46]. Figure 6b shows the corresponding isothermal entropy changes ( $\Delta S$ ) of the PBLZT AFE thick films as a function of temperature at  $\Delta E = 800$  kV/cm. The maximum  $\Delta S$  values are 9.8, 15.5 and 22.1 J/K/kg for the grain sizes of 0.19, 0.40 and 0.59  $\mu\text{m}$ , respectively. The large  $\Delta S$  of the PBLZT AFE thick film induces large ECE, making them suitable for refrigeration [46].

To comprehensively evaluate cooling performance of the PBLZT AFE thick films, Fig. 7 shows their coefficient of performance ( $COP$ ) and electrocaloric coefficient ( $\Delta T/\Delta E$ ) at different temperatures.  $COP$  is a measure to

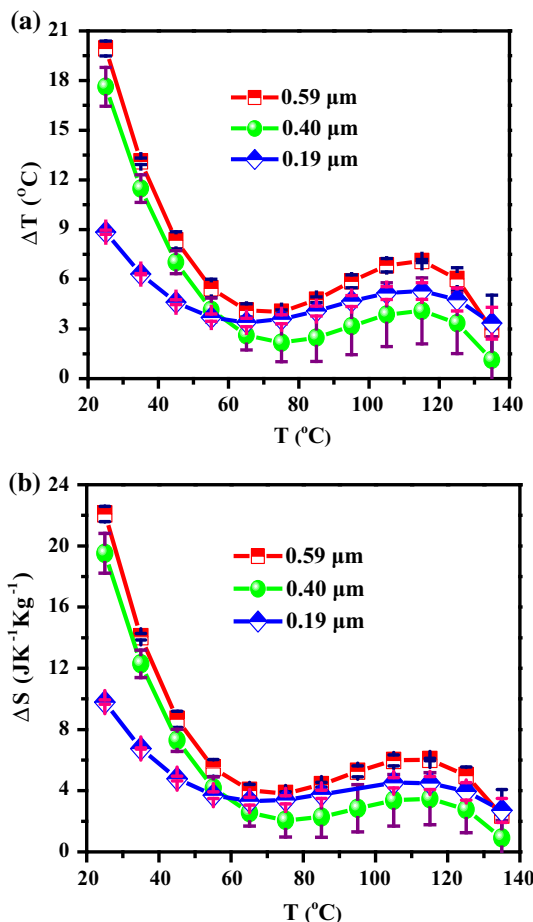
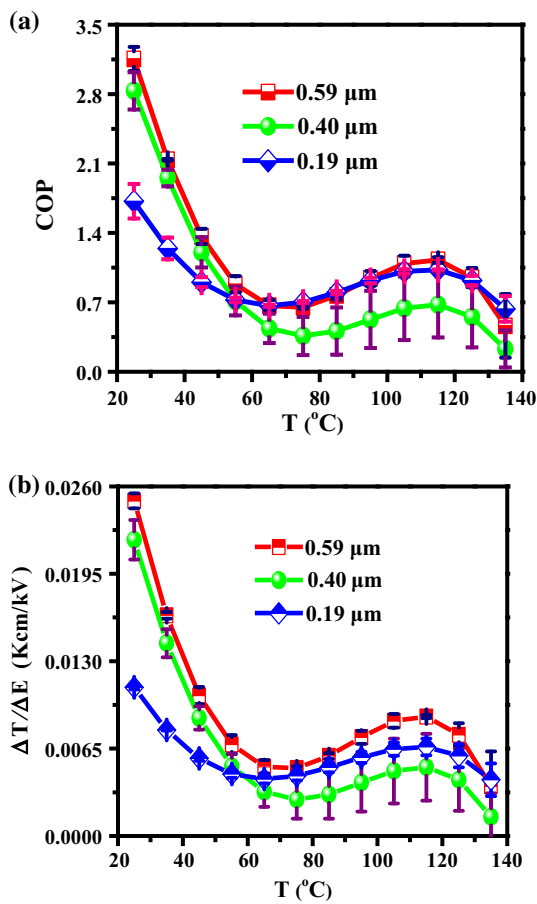


**Fig. 6** **a** Adiabatic temperature changes ( $\Delta T$ ) of the PBLZT AFE thick films with different grain sizes as a function of temperature at  $\Delta E = 800$  kV/cm. **b** Isothermal entropy changes ( $\Delta S$ ) as a function of temperature at  $\Delta E = 800$  kV/cm

evaluate the performance of a refrigeration cycle, which is defined as the ratio of the isothermal heat  $Q$  to  $W$  [47]:

$$COP = \frac{|Q|}{|W|} = \frac{|\Delta S \times T|}{|W|}, \tag{6}$$

where  $W$  is the recoverable energy density that is defined in the following part. At  $\Delta E = 800$  kV/cm,  $COP$  values of the PBLZT AFE thick films obtained with Eq. (6) are plotted in Fig. 7a. It is clear that all samples have a similar variation trend in  $COP$  in the measurement temperature range. The maximum  $COP$  values at room temperature are 1.7, 2.8 and 3.2, respectively. Figure 7b shows the corresponding electrocaloric coefficient ( $\Delta T/\Delta E$ ) of the PBLZT AFE thick films as a function of temperature. The values of  $\Delta T/\Delta E$  at room temperature are 0.011, 0.022 and 0.025 K cm/kV, respectively. The room temperature  $\Delta T/\Delta E$  value of the sample with grain size of 0.59  $\mu\text{m}$  is higher than that of ferroelectric ceramics [48–50].



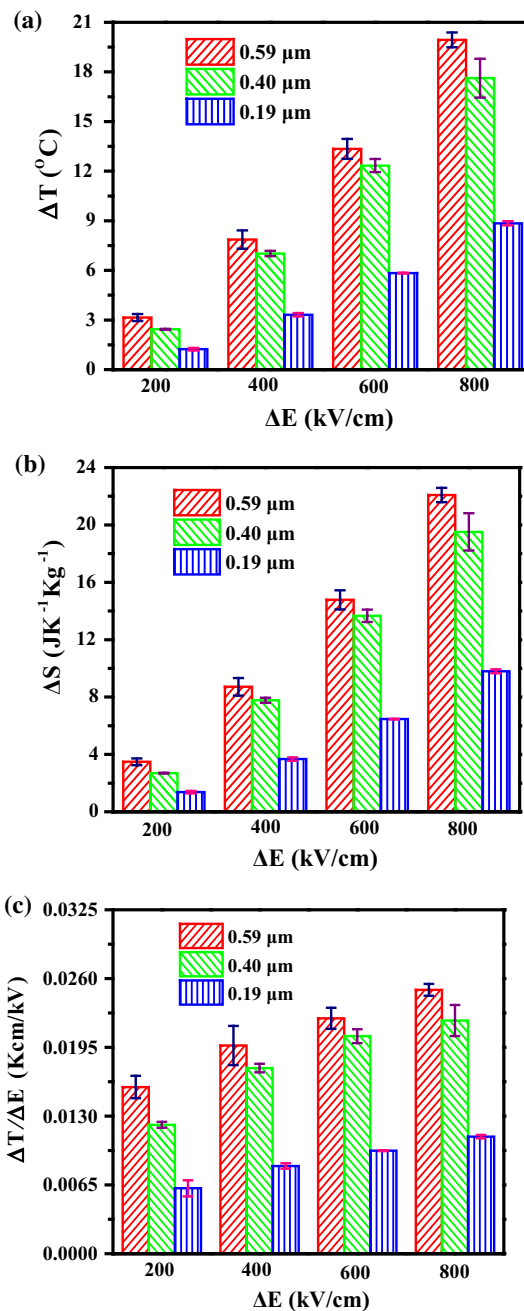
**Fig. 7** **a** Temperature dependences of refrigeration efficiency (*COP*) of the PBLZT AFE thick films with different grain sizes at  $\Delta E = 800$  kV/cm. **b** Corresponding electrocaloric coefficient of the films

Figure 8a shows room temperature  $\Delta T$  values of the PBLZT AFE thick films at  $\Delta E = 200, 400, 600$  and  $800$  kV/cm. It is obvious that the change in adiabatic temperature depends on not only grain size but also field change  $\Delta E$ . With the applied field increasing, adiabatic temperature change is increased. Therefore, to improve ECE, the electric field should be as high as possible.  $\Delta S$  and  $\Delta T/\Delta E$  at selected applied fields are shown in Fig. 8b, c. Obviously,  $\Delta S$  and  $\Delta T/\Delta E$  have the same variation trend as that of  $\Delta T$ .

ECE could also be evaluated by using the Landau thermodynamic theory. According to the thermodynamic phenomenological theory, Gibbs free energy in terms of polarization can be expanded as [51, 52]:

$$G = \frac{1}{2} \alpha P^2 + \frac{1}{2} \xi P^4 + \frac{1}{2} \varphi P^6, \tag{7}$$

where  $P \approx D$  ( $D = \epsilon_0 E + P$ , where  $\epsilon_0$  is vacuum dielectric permittivity,  $E$  is the applied field and  $P$  is the polarization),  $\alpha = \beta(T - T_0)$ , and  $\xi$  and  $\varphi$  are temperature independent coefficients. Since  $(\frac{\partial G}{\partial T})_P = -\Delta S$  [53], there is:



**Fig. 8** **a** Adiabatic temperature change ( $\Delta T$ ) of the PBLZT AFE thick films with different grain sizes at selected electric fields at room temperature. **b** Isothermal entropy changes ( $\Delta S$ ) of the films. **c** Electrocaloric coefficients of the films

$$\Delta S = -\frac{1}{2} \beta P^2, \tag{8}$$

where  $\beta$  is a phenomenological coefficient. Because  $-T\Delta S = c\Delta T$  ( $c$  is the specific heat capacity) [46], the temperature change can be obtained, which is given by:

$$\Delta T = -\frac{1}{2c} \beta T P^2, \tag{9}$$

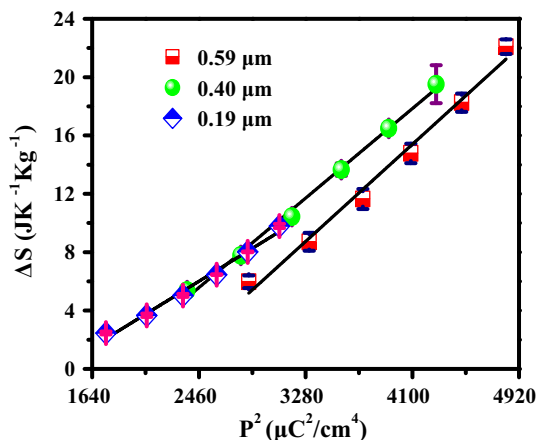
According to Eqs. (8) and (9), the entropy change and temperature change are proportional to square of the polarization. Moreover, a material with large  $\beta$  will generate larger entropy change and temperature change. As shown in Fig. 9, the entropy changes for the films have a linear relationship with the square of the polarization at room temperature. The values of  $\beta$  determined by linear fitting are  $9.13 \times 10^{-5}$ ,  $1.24 \times 10^{-4}$  and  $1.35 \times 10^{-4}$  J/cm/K/ $\mu\text{C}^2$  for the grain sizes of 0.19, 0.40 and 0.59  $\mu\text{m}$ , respectively. The values of the phenomenological coefficient  $\beta$  obtained in the present work are superior to the results of doped BaTiO<sub>3</sub> multilayer ceramic capacitor ( $4 \times 10^{-5}$  J/cm/K/ $\mu\text{C}^2$ ) [54] and BaTiO<sub>3</sub> single crystal ( $4 \times 10^{-5}$  J/cm/K/ $\mu\text{C}^2$ ) [55].

Figure 10a shows recoverable energy-storage density ( $W$ ) and energy-storage efficiency ( $\eta$ ) of the PBLZT AFE thick films, at different applied electric fields at 1 kHz and at room temperature. They are calculated according to their definition [22, 56–59]:

$$W = \int_{P_r}^{P_{\max}} EdP, \tag{10}$$

$$\eta = \frac{W}{W + W_{\text{loss}}}, \tag{11}$$

where  $E$  is applied electric field,  $P$  is the polarization,  $P_r$  is the remanent polarization and  $P_{\max}$  is the maximum polarization with respect to the maximum experimental electric field.  $W_{\text{loss}}$  represents the energy loss density, which is obtained by integrating the area between the charge and discharge curves. Evidently, larger grain size leads to a higher energy density at the same electric field. This could be contributed to the increased difference between  $P_{\max}$  and  $P_r$ . Moreover, as expected, the energy-storage density of all the samples monotonically increases



**Fig. 9** Isothermal entropy change ( $\Delta S$ ) of the PBLZT AFE thick films with different grain sizes as a function of polarization at room temperature

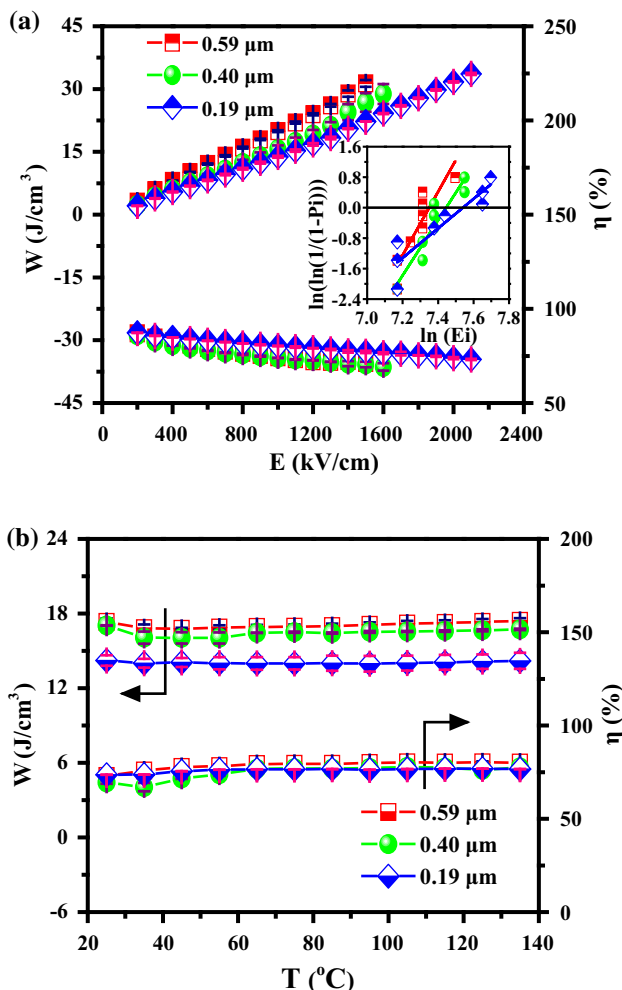
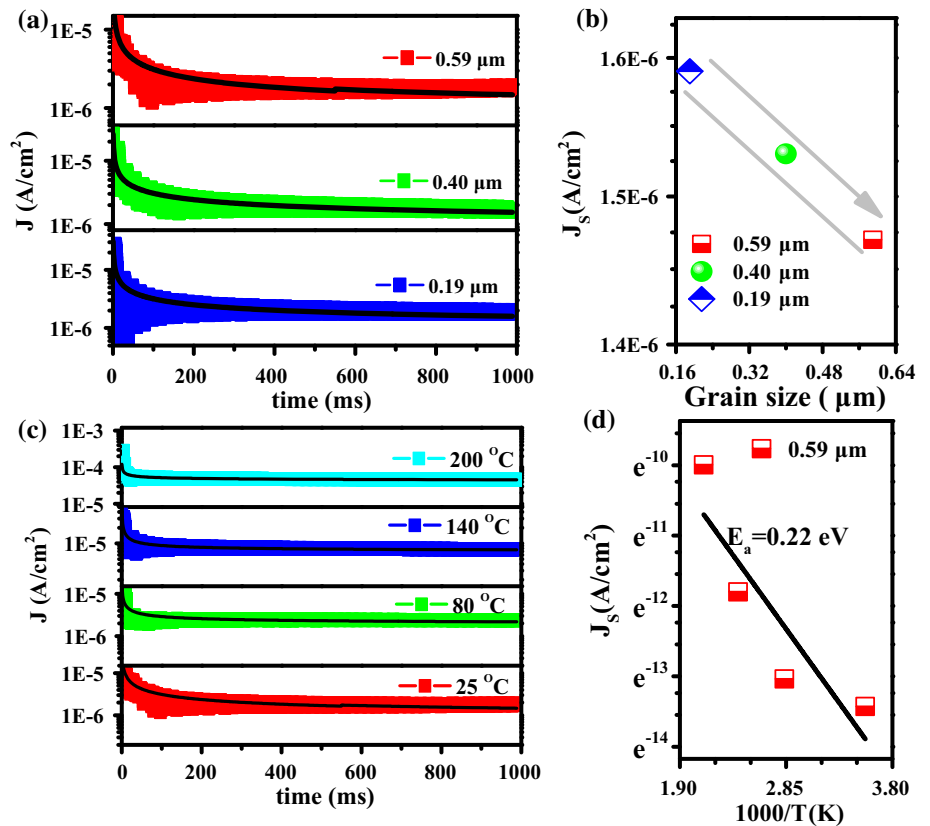


**Fig. 10** **a** Electric-field dependences of recoverable energy-storage density and energy-storage efficiency of the PBLZT AFE thick films with different grain sizes, with the inset showing the Weibull distribution and the fitting lines of breakdown strength of the films. **b** Temperature dependences of energy-storage density and energy storage efficiency of the films measured at 1000 kV/cm

with increasing applied electric field, before reaching the breakdown fields. The inset in Fig. 10a gives Weibull distribution of breakdown strength (BDS) of the AFE thick films [60, 61]. According to the data given in the inset, BDS values of the films with grain sizes of 0.19, 0.40 and 0.59  $\mu\text{m}$  obtained from the x intercept of the fitting lines are 1882, 1712 and 1556 kV/cm, respectively. This result indicated that films with smaller grain size have higher breakdown fields. The recoverable energy-storage densities at their corresponding BDS are 33.6, 28.8, and 31.4 J/cm<sup>3</sup> for the films with grain sizes of 0.19, 0.40 and 0.59  $\mu\text{m}$ , respectively. For practical applications, besides high energy density  $W$ , large energy-storage efficiency ( $\eta$ ) is also important. Clearly, all films have an efficiency of more than 70 %, which slightly decrease with increasing electric



**Fig. 11** **a** Dielectric relaxation currents of the PBLZT AFE thick films with different grain sizes, at 400 kV/cm and room temperature. **b** Steady-state leakage current of the films. **c** Dielectric relaxation currents of the thick films with a grain size of 0.59 μm at different temperatures. **d** Steady-state leakage current versus temperature of the films



field. For example, the maximum  $\eta$  of 73 % is obtained in the thick films with a grain size of 0.19 μm.

Temperature stability of energy-storage performance is also an important parameter for practical applications [62]. Figure 10b shows temperature dependence of energy-storage performance of the PBLZT AFE thick films over 25–135 °C at 1 kHz at 1000 kV/cm. In the temperature range, all the curves are only slightly fluctuated, indicating excellent temperature stability of energy-storage performance of the thick films.

Figure 11a shows current characteristics of the PBLZT AFE thick films, as a function of time, at  $E = 400$  kV/cm at room temperature. It was reported that the decay of dielectric relaxation current obeys the Curie–von Schweidler law [63]:

$$J = J_s + J_0 \times t^{-n}, \tag{12}$$

where  $J_s$  is the steady-state current density,  $J_0$  is a fitting constant,  $t$  is the relaxation time in seconds, and  $n$  is the slope of the log–log plot. By fitting the leakage current density data according to Eq. (12),  $J_s$  values at  $E = 400$  kV/cm are  $1.59 \times 10^{-6}$ ,  $1.53 \times 10^{-6}$  and  $1.47 \times 10^{-6}$  A/cm<sup>2</sup>, respectively, as shown in Fig. 11b. The small leakage current is very close to that of other lead-based AFE thick films [8, 31]. Moreover, it can be

found that the steady-state leakage current density is decreased with increasing grain size. As an example, Fig. 11c shows temperature-dependent current characteristics of the 0.59 μm film, at  $E = 400$  kV/cm. Obviously, the current density of the sample is increased with the operating temperature increasing. The data of the temperature-dependent  $J_s$  were fitted to the Arrhenius equation [64]:

$$J_s = A \exp\left(-\frac{E_a}{kT}\right), \tag{13}$$

where  $A$ ,  $E_a$  and  $k$  are fitting constant, activation energy and Boltzmann constant, respectively. According to the fitting curve shown in the inset of Fig. 11d, the result yields an activation energy of  $\sim 0.22$  eV for the 0.59 μm film, which is close to the results of PLZST AFE thick films [31] and PLZT AFE thin films [14].

### 4 Conclusions

Through proper control of annealing time, (100)-oriented PBLZT AFE thick films with different grain sizes were successfully fabricated by using a sol–gel route. The grain size had a strong influence on dielectric properties of the

AFE thick films. With increasing grain size, both dielectric constant and polarization were increased, but breakdown field was decreased. All the films showed a diffused phase transition behavior. As a result, AFE thick films with larger grain size showed improved ECE. The film with a grain size of 0.59  $\mu\text{m}$  exhibited highest ECE performance, with  $\Delta T = 19.9\text{ }^\circ\text{C}$  and  $\Delta S = 22.1\text{ J/K/kg}$ , leading to electrocaloric coefficient and refrigeration efficiency of 0.025 K/cm/kV and 3.2. However, due to its higher breakdown field, the film with a grain size of 0.19  $\mu\text{m}$  possessed a maximum recoverable energy-storage density of 33.6 J/cm<sup>3</sup> and an efficiency of 73 %. Promising thermal energy-storage stability was observed in the films due to their diffused phase transition and very low leakage current. Therefore, it is believed that our PBLZT AFE thick films are promising candidates for applications in solid-cooling devices and energy-storage capacitors.

**Acknowledgments** The authors would like to acknowledge the financial support by the Ministry of Sciences and Technology of China through 973-Project (2014CB660811), the National Natural Science Foundation of China (51462027), the Program for Innovative Research Team in Universities of Inner Mongolia Autonomous Region (NMGIRT-A1605), the Innovation Guide Fund of Baotou (CX2015-8) and the Innovation Program of Inner Mongolia University of Science and Technology (2014QNGG01).

## References

1. C. Kittel, Theory of antiferroelectric crystal. *Phys. Rev.* **82**, 729–732 (1951)
2. E. Sawaguchi, H. Maniwa, S. Hoshino, Antiferroelectric structure of lead zirconate. *Phys. Rev.* **83**, 1078 (1951)
3. G. Shirane, E. Sawaguchi, Y. Takagi, Dielectric properties of lead zirconate. *Phys. Rev.* **84**, 476–481 (1951)
4. X.H. Hao, Y. Wang, L. Zhang, L.W. Zhang, S.L. An, Composition-dependent dielectric and energy-storage properties of (Pb, La)(Zr, Sn, Ti)O<sub>3</sub> antiferroelectric thick films. *Appl. Phys. Lett.* **102**, 163903 (2013)
5. Z. Liu, X.F. Chen, W. Peng, C.H. Xu, X.L. Dong, F. Cao, G.S. Wang, Temperature-dependent stability of energy storage properties of Pb<sub>0.97</sub>La<sub>0.02</sub>(Zr<sub>0.58</sub>Sn<sub>0.335</sub>Ti<sub>0.085</sub>)O<sub>3</sub> antiferroelectric ceramics for pulse power capacitors. *Appl. Phys. Lett.* **106**, 262901 (2015)
6. Z.K. Xu, J.W. Zhai, W.H. Chan, Phase transformation and electric field tunable pyroelectric behavior of Pb(Nb, Zr, Sn, Ti)O<sub>3</sub> and (Pb, La)(Zr, Sn, Ti)O<sub>3</sub> antiferroelectric thin films. *Appl. Phys. Lett.* **88**, 132908 (2006)
7. S.S. Sengupta, D. Roberts, J.F. Li, M.C. Kim, D.A. Payne, Field-induced phase switching and electrical driven strains in sol-gel derived antiferroelectric (Pb, Nb)(Zr, Sn, Ti)O<sub>3</sub> thin films. *J. Appl. Phys.* **78**, 1171–1177 (1995)
8. Y. Zhao, X.H. Hao, Q. Zhang, Energy-storage properties and electrocaloric effect of Pb<sub>(1-3x/2)</sub>La<sub>x</sub>Zr<sub>0.85</sub>Ti<sub>0.15</sub>O<sub>3</sub> antiferroelectric thick films. *ACS Appl. Mater. Interfaces* **6**, 11633–11639 (2014)
9. X.H. Hao, J.W. Zhai, L.B. Kong, Z.K. Xu, A comprehensive review on the progress of lead zirconate-based antiferroelectric materials. *Prog. Mater. Sci.* **63**, 1–57 (2014)
10. J. Ge, X.L. Dong, Y. Chen, F. Cao, G.S. Wang, Enhanced polarization switching and energy storage properties of Pb<sub>0.97</sub>La<sub>0.02</sub>(Zr<sub>0.95</sub>Ti<sub>0.05</sub>)O<sub>3</sub> antiferroelectric thin films with LaNiO<sub>3</sub> oxide top Electrodes. *Appl. Phys. Lett.* **102**, 142905 (2013)
11. M. Valant, Electrocaloric materials for future solid-state refrigeration technologies. *Prog. Mater. Sci.* **57**, 980–1009 (2012)
12. G.Z. Zhang, D.Y. Zhu, X.S. Zhang, L. Zhang, J.Q. Yi, B. Xie, Y.K. Zeng, Q. Li, Q. Wang, S.L. Jiang, High-energy storage performance of (Pb<sub>0.87</sub>Ba<sub>0.1</sub>La<sub>0.02</sub>)(Zr<sub>0.68</sub>Sn<sub>0.24</sub>Ti<sub>0.08</sub>)O<sub>3</sub> antiferroelectric ceramics fabricated by the hot-press sintering method. *J. Am. Ceram. Soc.* **4**, 1175–1181 (2015)
13. B.A. Tuttle, D.A. Payne, The effects of microstructure on the electrocaloric properties of Pb(Zr, Sn, Ti)O<sub>3</sub> ceramics. *Ferroelectrics* **37**, 603–606 (1981)
14. Z.Q. Hu, B.H. Ma, R.E. Koritala, U. Balachandran, Temperature-dependent energy storage properties of antiferroelectric Pb<sub>0.96</sub>La<sub>0.04</sub>Zr<sub>0.98</sub>Ti<sub>0.02</sub>O<sub>3</sub> thin films. *Appl. Phys. Lett.* **104**, 263902 (2014)
15. J. Parui, S.B. Krupanidhi, Electrocaloric effect in antiferroelectric PbZrO<sub>3</sub> thin films. *Phys. Status Solidi RRL* **2**, 230–232 (2008)
16. X.F. Chen, F. Cao, H.L. Zhang, G. Yu, G.S. Wang, X.L. Dong, Y. Gu, H.L. He, Y.S. Liu, Dynamic hysteresis and scaling behavior of energy density in dynamic hysteresis and scaling behavior of energy density in Pb<sub>0.99</sub>Nb<sub>0.02</sub>[(Zr<sub>0.60</sub>Sn<sub>0.40</sub>)<sub>0.95</sub>Ti<sub>0.05</sub>]O<sub>3</sub> Antiferroelectric bulk ceramics. *J. Am. Ceram. Soc.* **4**, 1163–1166 (2012)
17. S. Kar-Narayan, N.D. Mathur, Predicted cooling powers for multilayer capacitors based on various electrocaloric and electrode materials. *Appl. Phys. Lett.* **95**, 242903 (2009)
18. J. Ge, D. Remiens, J. Costecalde, Y. Chen, X.L. Dong, G.S. Wang, Effect of residual stress on energy storage property in PbZrO<sub>3</sub> antiferroelectric thin films with different orientations. *Appl. Phys. Lett.* **103**, 162903 (2013)
19. B.L. Peng, H.Q. Fan, Q. Zhang, A. Giant, Electrocaloric effect in nanoscale antiferroelectric and ferroelectric phases coexisting in a relaxor Pb<sub>0.8</sub>Ba<sub>0.2</sub>ZrO<sub>3</sub> thin film at room temperature. *Adv. Funct. Mater.* **23**, 2987–2992 (2013)
20. X.H. Hao, J.W. Zhai, Electric-field tunable electrocaloric effects from phase transition between antiferroelectric and ferroelectric phase. *Appl. Phys. Lett.* **104**, 022902 (2014)
21. J. Ge, G. Pan, D. Remiens, Y. Chen, F. Cao, X.L. Dong, G.S. Wang, Effect of electrode materials on the scaling behavior of energy density in Pb(Zr<sub>0.96</sub>Ti<sub>0.03</sub>)Nb<sub>0.01</sub>O<sub>3</sub> antiferroelectric films. *Appl. Phys. Lett.* **101**, 112905 (2012)
22. B.L. Peng, Q. Zhang, X. Li, T.Y. Sun, H.Q. Fan, S.M. Ke, M. Ye, Y. Wang, W. Lu, H.B. Niu, J.F. Scott, X.R. Zeng, H.T. Huang, Giant electric energy density in epitaxial lead-free thin films with coexistence of ferroelectrics and antiferroelectrics. *Adv. Electron. Mater.* **1**, 1–7 (2015)
23. F.L. Goupil, A.K. Axelsson, L.J. Dunne, M. Valant, G. Manos, T. Lukasiewicz, J. Dec, A. Berenov, N.M. Alford, Anisotropy of the electrocaloric effect in lead-free relaxor ferroelectrics. *Adv. Energy Mater.* **4**, 1301688 (2014)
24. L. Zhang, S.L. Jiang, Y.K. Zeng, M. Fu, K. Han, Q. Li, Q. Wang, G.Z. Zhang, Y doping and grain size co-effects on the electrical energy storage performance of (Pb<sub>0.87</sub>Ba<sub>0.1</sub>La<sub>0.02</sub>)(Zr<sub>0.65</sub>Sn<sub>0.3</sub>Ti<sub>0.05</sub>)O<sub>3</sub> anti-ferroelectric ceramics. *Ceram. Int.* **40**, 5455–5460 (2014)
25. J.H. Qiu, Q. Jiang, Grain size effect on the electrocaloric effect of dense BaTiO<sub>3</sub> nanoceramics. *J. Appl. Phys.* **105**, 034110 (2009)
26. C. Fang, D.X. Zhou, S.P. Gong, Core-shell structure and size effect in barium titanate nanoparticle. *Phys. B* **406**, 1317–1322 (2011)
27. M. Vrabelj, H. Uršič, Z. Kutnjak, B. Rožič, S. Drnovšek, A. Benčan, V. Bobnar, L. Fulanović, B. Malič, Large electrocaloric

- effect in grain-size-engineered  $0.9\text{Pb}(\text{Mg}_{1/3}\text{Nb}_{2/3})\text{O}_3-0.1\text{PbTiO}_3$ . *J. Eur. Ceram. Soc.* **36**, 75–80 (2016)
28. H.F. Ji, W. Ren, L.Y. Wang, P. Shi, X.F. Chen, X.Q. Wu, X. Yao, S.T. Lau, Q.F. Zhou, K.K. Shung, Structure and electrical properties of  $\text{Na}_{0.5}\text{Bi}_{0.5}\text{TiO}_3$  ferroelectric thick films derived from a polymer modified sol–gel method. *IEEE Trans. Ultrason. Ferroelectr. Freq. Control* **58**, 2042–2049 (2011)
  29. J.W. Zhai, X. Li, Y. Yao, H. Chen, Growth and characterization of PNZST thin films. *Mater. Sci. Eng., B* **99**, 230–233 (2003)
  30. J.K. Li, X. Yao, Microstructure and electrical properties of  $\text{Pb}(\text{Zr}_{0.52}\text{Ti}_{0.48})\text{O}_3$  ferroelectric films on different bottom electrodes. *Mater. Lett.* **58**, 3447–3450 (2004)
  31. X.H. Hao, Y. Zhao, Q. Zhang, Phase structure tuned electrocaloric effect and pyroelectric energy harvesting performance of  $(\text{Pb}_{0.97}\text{La}_{0.02})(\text{Zr}, \text{Sn}, \text{Ti})\text{O}_3$  antiferroelectric thick films. *J. Phys. Chem. C* **119**, 18877–18885 (2015)
  32. C.R. Cho, W.J. Lee, B.G. Yu, B.W. Kim, Dielectric and ferroelectric response as a function of annealing temperature and film thickness of sol-gel deposited  $\text{PbZr}_{0.52}\text{Ti}_{0.48}\text{O}_3$  thin film. *J. Appl. Phys.* **86**, 2700–2711 (1999)
  33. J. Yu, X.J. Meng, J.L. Sun, Z.M. Huang, J.H. Chu, Optical and electrical properties of highly (100)-oriented  $\text{PbZr}_{1-x}\text{Ti}_x\text{O}_3$  thin films on the  $\text{LaNiO}_3$  buffer layer. *J. Appl. Phys.* **96**, 2792–2799 (2004)
  34. C. Bhardwaj, B.S.S. Daniela, D. Kaur, Pulsed laser deposition and characterization of highly tunable  $(1-x)\text{Ba}(\text{Zr}_{0.2}\text{Ti}_{0.8})\text{O}_3-x(\text{Ba}_{0.7}\text{Ca}_{0.3})\text{TiO}_3$  thin films grown on  $\text{LaNiO}_3/\text{Si}$  substrate. *J. Phys. Chem. Solids* **74**, 94–100 (2013)
  35. S.B. Kang, M.G. Choi, D.J. Jeong, Energy storage properties of nano-grained antiferroelectric  $(\text{Pb}, \text{La})(\text{Zr}, \text{Ti})\text{O}_3$  films prepared by aerosol-deposition method. *IEEE Trans. Dielect. Electr. Insul.* **22**, 1477–1482 (2015)
  36. J.S. Lee, S.K. Joo, Analysis of grain-boundary effects on the electrical properties of  $\text{Pb}(\text{Zr}, \text{Ti})\text{O}_3$  thin films. *Appl. Phys. Lett.* **81**, 2602–2604 (2002)
  37. X.G. Tang, H.L.W. Chan, Effect of grain size on the electrical properties of  $(\text{Ba}, \text{Ca})(\text{Zr}, \text{Ti})\text{O}_3$  relaxor ferroelectric ceramic. *J. Appl. Phys.* **97**, 034109 (2005)
  38. X.G. Tang, K.H. Chew, H.L.W. Chan, Diffuse phase transition and dielectric tunability of  $\text{Ba}(\text{Zr}_y\text{Ti}_{1-y})\text{O}_3$  relaxor ferroelectric ceramics. *Acta Mater.* **52**, 5177–5183 (2004)
  39. B. Pokharel, D. Pandey, Dielectric studies of phase transitions in  $(\text{Pb}_{1-x}\text{Ba}_x)\text{ZrO}_3$ . *J. Appl. Phys.* **88**, 5364–5373 (2000)
  40. K. Uchino, S. Nomura, Critical exponents of the dielectric costants in diffused-phase-transition crystals. *Ferroelectrics* **44**, 55–61 (1982)
  41. V.S. Tiwari, N. Singh, D. Pandey, Diffuse ferroelectric transition and relaxational dipolar freezing in  $(\text{Ba}, \text{Sr})\text{TiO}_3$ . *J. Phys. Condens. Matter.* **7**, 1441–1460 (1995)
  42. W.L. Zhao, R.Z. Zuo, D.G. Zheng, L.T. Li, Dielectric relaxor evolution and frequency-insensitive giant strains in  $(\text{Bi}_{0.5}\text{Na}_{0.5})\text{TiO}_3$ -Modified  $\text{Bi}(\text{Mg}_{0.5}\text{Ti}_{0.5})\text{O}_3$ - $\text{PbTiO}_3$  Ferroelectric Ceramics. *J. Am. Ceram. Soc.* **97**, 1855–1860 (2014)
  43. K. Wen, J.H. Qiu, H.L. Ji, K.J. Zhu, J.S. Liu, J. Wang, J.Z. Du, F.L. Zhu, Investigation of phase diagram and electrical properties of  $x\text{Pb}(\text{Mg}_{1/3}\text{Nb}_{2/3})\text{O}_3-(1-x)\text{Pb}(\text{Zr}_{0.4}\text{Ti}_{0.6})\text{O}_3$  ceramics. *J. Mater. Sci. Mater. Electron.* **25**, 3003–3009 (2014)
  44. A.S. Mischenko, Q. Zhang, J.F. Scott, R.W. Whatmore, N.D. Mathur, Giant electrocaloric effect in thin-film  $\text{PbZr}_{0.95}\text{Ti}_{0.05}\text{O}_3$ . *Science* **311**, 1270–1271 (2006)
  45. T. Mitsui, I. Tatsuzaki, E. Nakamura, *An Introduction to the Physics of Ferroelectrics* (Gordon and Breach, London, 1976)
  46. S.G. Lu, Q.M. Zhang, Electrocaloric materials for solid-state refrigeration. *Adv. Mater.* **21**, 1983–1987 (2009)
  47. E. Defay, S. Crossley, S. Kar-Narayan, X. Moya, N.D. Mathur, The electrocaloric efficiency of ceramic and polymer films. *Adv. Mater.* **25**, 3337–3342 (2013)
  48. J. Hagberg, A. Uusimäki, H. Jantunen, Electrocaloric characteristics in reactive sintered  $0.87\text{Pb}(\text{Mg}_{1/3}\text{Nb}_{2/3})\text{O}_3-0.13\text{PbTiO}_3$ . *Appl. Phys. Lett.* **92**, 132909 (2008)
  49. Y. Bai, X. Han, L.J. Qiao, Optimized electrocaloric refrigeration capacity in lead-free  $(1-x)\text{BaZr}_{0.2}\text{Ti}_{0.8}\text{O}_3-x\text{Ba}_{0.7}\text{Ca}_{0.3}\text{TiO}_3$  ceramics. *Appl. Phys. Lett.* **103**, 202903 (2013)
  50. X.Q. Liu, T.T. Chen, Y.J. Wu, X.M. Chen, Enhanced electrocaloric effects in spark plasma-sintered  $\text{Ba}_{0.65}\text{Sr}_{0.35}\text{TiO}_3$ -based ceramics at room temperature. *J. Am. Ceram. Soc.* **96**, 1021–1023 (2013)
  51. S. Lu, B. Rožič, Q.M. Zhang, Z. Kutnjak, X.Y. Li, E. Furman, L.J. Gorny, M. Lin, B. Malič, M. Kosec, R. Blinc, R. Pirc, Organic and inorganic relaxor ferroelectrics with giant electrocaloric effect. *Appl. Phys. Lett.* **97**, 162904 (2010)
  52. S.G. Lu, B. Rozic, Q.M. Zhang, Z. Kutnjak, R. Pirc, Electrocaloric effect in ferroelectric polymers. *Appl. Phys. A Mater.* **107**, 559–566 (2012)
  53. M. Lines, A. Glass, *Principles and Applications of Ferroelectrics and Related Materials* (Clarendon Press, Oxford, 1977)
  54. S. Kar-Narayan, N.D. Mathur, Direct and indirect electrocaloric measurements using multilayer capacitors. *J. Phys. D Appl. Phys.* **43**, 032002 (2010)
  55. X. Moya, E. Stern-Taulats, S. Crossley, D. González-Alonso, S. Kar-Narayan, A. Planes, L. Mañosa, N.D. Mathur, Giant electrocaloric strength in single-crystal  $\text{BaTiO}_3$ . *Adv. Mater.* **25**, 1360–1365 (2013)
  56. B.J. Chu, X. Zhou, K.L. Ren, B. Neese, M.R. Lin, Q. Wang, F. Bauer, Q.M. Zhang, A dielectric polymer with high electric energy density and fast discharge speed. *Science* **313**, 334–336 (2006)
  57. Z.B. Shen, X.H. Wang, B.C. Luo, L.T. Li,  $\text{BaTiO}_3$ - $\text{BiYbO}_3$  perovskite materials for energy storage applications. *J. Mater. Chem. A* **3**, 18146–18153 (2015)
  58. B.L. Peng, Q. Zhang, X. Li, T.Y. Sun, H.Q. Fan, S.M. Ke, M. Ye, Y. Wang, W. Lu, H.B. Niu, X.R. Zhang, H.T. Huang, Large energy storage density and high thermal stability in a highly textured (111)-oriented  $\text{Pb}_{0.8}\text{Ba}_{0.2}\text{ZrO}_3$  Relaxor thin film with the coexistence of antiferroelectric and ferroelectric phases. *ACS Appl. Mater. Interfaces* **7**, 13512–13517 (2015)
  59. M.H. Park, Y.H. Lee, H.J. Kim, Y.J. Kim, T. Moon, K.D. Kim, J. Müller, A. Kersch, U. Schroeder, T. Mikolajick, C.S. Hwang, ferroelectricity and antiferroelectricity of doped thin  $\text{HfO}_2$ -based films. *Adv. Mater.* **27**, 1811–1831 (2015)
  60. Y. Zhao, X.H. Hao, M. Li, Dielectric properties and energy-storage performance of  $(\text{Na}_{0.5}\text{Bi}_{0.5})\text{TiO}_3$  thick films. *J. Alloys Compd.* **601**, 112–115 (2014)
  61. Y. Wang, Y.C. Chan, Z.L. Gui, D.P. Webb, L.T. Li, Application of weibull distribution analysis to the dielectric failure of multilayer ceramic capacitors. *Mater. Sci. Eng. B* **47**, 197–203 (1997)
  62. X.L. Wang, L. Zhang, X.H. Hao, S.L. An, High energy-storage performance of  $0.9\text{Pb}(\text{Mg}_{1/3}\text{Nb}_{2/3})\text{O}_3-0.1\text{PbTiO}_3$  relaxor ferroelectric thin films prepared by RF magnetron sputterin. *Mater. Res. Bull.* **65**, 73–79 (2015)
  63. S. Tong, B.H. Ma, M. Narayanan, S.S. Liu, R.E. Koritala, U. Balachandran, D.L. Shi, Lead lanthanum zirconate titanate ceramic thin films for energy storage. *ACS Appl. Mater. Interfaces* **5**, 1474–1480 (2013)
  64. B.H. Ma, S. Chao, M. Narayanan, S.S. Liu, S. Tong, R.E. Koritala, U. Balachandran, Dense PLZT films grown on nickel substrates by PVP-modified sol–gel method. *J. Mater. Sci.* **48**, 1180–1185 (2013)